https://doi.org/10.1038/s44384-025-00026-5

Simultaneous acoustic perfect absorption and rainbow trapping via topologically optimized sub-wavelength multi-slit sonic crystal metamaterials

Wai Kit Lam[1] ✉, Anton Krynkin[2], Olga Umnova[3] & Shiu Keung Tang[4]

Acoustic perfect absorption at 500 Hz and across the low-frequency range of 400–1000 Hz is demonstrated using a metamaterial structure composed of graded sub-wavelength multi-slit sonic crystal (MSSC) elements designed through a topology optimization framework that integrates a genetic algorithm with a novel effective medium approach, rigorously accounting for visco-thermal losses in the slits via Stinson's model, avoiding reliance on artificial loss factors. The effective impedances of the unit cells embedding each MSSC element are precisely tuned to match the surrounding medium, thereby satisfying the critical coupling condition for optimal absorption. Remarkably, the optimized structure exhibits spatially graded acoustic properties that sequentially localize energy at designated frequencies, producing the rainbow-trapping phenomenon. Notably, the largest element measures only 7 cm in diameter—deeply sub-wavelength at about 1/12 the wavelength at 400 Hz. The proposed design and methodology offer promising applications in acoustic filtering, energy harvesting, and noise mitigation, particularly in ventilation systems.

In recent decades, the emergence of acoustic metamaterials (AMMs) has opened new pathways for unprecedented acoustic wave manipulation. By carefully designing the geometry and arrangement of sub-wavelength elements, AMMs have demonstrated remarkable capabilities in controlling sound waves, including the realization of perfect absorption. Various sub-wavelength structures, such as meta-membranes[1,2], space-coiled materials[3–6], quarter-wavelength resonators[7,8], Helmholtz resonators[9–13], coupled surface-resonator[14,15], and bubble meta-screen[16,17], have been reported to exhibit near-perfect absorption at targeted frequencies by leveraging the slowing-down effect of sound at resonance and the coupling among constitutive elements, which cause strong dispersion and energy localization near resonance frequencies.

However, these structures often suffer from limitations such as narrow operational bandwidths, weak coupling effects between elements, or geometrical complexity, thereby impeding the realization of broadband perfect absorption.

To overcome these limitations and improve absorption performance, researchers have explored a variety of innovative designs. Examples such as sub-wavelength acoustic panels[18], meta-surfaces[19,20], micro-perforated panels combined with coiled-up cavities[21,22], and coiled Fabry-Perot channels[23,24], have demonstrated the ability to achieve broadband near-perfect absorption through impedance matching between different media and by satisfying the critical coupling condition – where the intrinsic visco-thermal losses are balanced with energy leakage at resonance[18] – over a much wider frequency range. Additionally, the overlap of multiple local resonance bandgaps has been shown to further improve broadband absorption characteristics.

Notably, in conjunction with broadband absorption, the acoustic rainbow trapping phenomenon arising from the unique dispersive and graded properties of metamaterial has simultaneously been discovered in several acoustic structures[18,25–27]. The strategically designed spatial variations in these metamaterial geometries cause different frequency components of the incoming wave to propagate at different phase velocities. As a result, these frequency components become spatially separated and locally trapped at different positions within the structure, leading to broadband energy confinement and the well-known rainbow trapping effect.

It is worth noting that the earliest demonstration of this phenomenon can be traced back to an optical setting. In 2007 Tsakmakidis et al.[28]

[1]Department of Building Environment and Energy Engineering, The Hong Kong Polytechnic University, Hung Hom, Hong Kong SAR, China. [2]School of Mechanical, Aerospace and Civil Engineering, The University of Sheffield, Sheffield, UK. [3]Acoustics Research Centre, University of Salford, Salford, Greater Manchester, UK. [4]Department of Mechanical and Aerospace Engineering, United Arab Emirates University, Al Ain, United Arab Emirates. ✉e-mail: wai-kit-adrian.lam@connect.polyu.hk

employed a left-handed heterostructure to stop and store light. The concept has been extended beyond acoustics and optics to other wave domains, including elastic waves[29], and water waves[30], highlighting its versatility and potential across diverse physical settings.

Moreover, the rainbow trapping phenomenon is also present in biological systems such as the mammalian cochlea. The cochlea leverages graded material properties to achieve spatial separation of frequencies, effectively implementing a natural form of graded resonances. An overview of this mechanism and its relation to metamaterial principles is provided in ref. 31. Inspired by this biological paradigm, several studies have developed graded acoustic metamaterials that closely mimic cochlear functionality using arrays of passive or active resonators[32–36], marking a specialized and biologically informed direction within the metamaterials community.

From a practical standpoint, the simultaneous realization of tuneable rainbow trapping and broadband perfect absorption within a single metamaterial system holds significant promise for transformative applications across various acoustic domains, such as energy harvesting[37], focusing[38], imaging[39], and the effective mitigation of low-frequency noise in architectural features like ventilation windows and ducts[40,41], where both transmission and reflection are undesirable.

Despite these advances, it is important to note that the geometrical parameters of many previously reported metamaterial designs are often determined through manual tuning or intuition-based selection. This lack of a systematic methodology limits the ability to effectively and systematically explore the design space. For structures involving multiple elements – as typically required for achieving broadband absorption and rainbow trapping – manual parameter selection becomes increasingly labour-intensive and oftentimes suboptimal.

While a few systematic optimization schemes have been proposed for non-graded metamaterials, such as those in refs. 42–44, these approaches are typically FEM-assisted, relying on real-time FEM simulations as input to the optimization algorithm in each iteration. Such FEM-based methods are known to be computationally expensive due to the need for dense meshing to ensure accuracy, the geometric complexity of the models, and the large number of iterations required by the optimization process. Furthermore, these methods often face challenges in maintaining geometric parameter continuity, as the geometries are always required to be discretized and represented as binary matrices for compatibility and communication between FEM simulations and numerical solvers such as MATLAB during optimization. This issue becomes particularly pronounced when dealing with complex geometries, potentially undermining both the quality and generalizability of the optimized designs. Also, in some cases, if discretization constraints – such as pixel connectivity or force distribution – are not properly defined, the resulting 'optimized' structures may actually be physically unrealistic or impractical for real-world applications.

In the context of graded metamaterials, several studies have successfully employed more efficient optimization strategies, often combined with analytical approaches and sometimes without the aid of FEM. For instance, in ref. 18, Jiménez et al. achieved broadband perfect absorption and rainbow trapping at low frequencies using a graded array of rectangular Helmholtz resonators with single openings, mounted along the upper boundary of a waveguide. Their approach represents each resonator using a single matrix that also accounts for inherent visco-thermal losses, allowing for the direct computation of the absorption coefficient from a global matrix system.

Similarly, in ref. 30, Wilks et al. extended the concept to linear water waves using a graded array of submerged vertical barriers. They formulated the approximated scattering matrix through the solution of an integral equation system using the Galerkin method, which allowed them to efficiently evaluate the overall performance of the barrier array. Based on these results, they employed a modified optimization algorithm (also discussed in ref. 18), enabling highly effective optimization.

In the domain of elastic waves, analogous effects of wave confinement and amplification were demonstrated by Rosafalco et al.[29] using an array of resonators attached to an elastic plate. Notably, their design geometrical parameters were optimized using a reinforcement learning framework based on a Markov decision process. While FEM simulations were still required to assist in training the model, their innovative application of machine learning to metamaterial design highlights the growing potential of advanced AI-based optimization techniques for discovering high-performance meta-structures.

Therefore, motivated by these developments, and recognizing the limitations of the existing approaches, in this study, we introduce a compact and efficient acoustic metamaterial in the form of graded multi-slit sonic crystals (MSSCs), designed to achieve both single-frequency perfect absorption at 500 Hz and broadband perfect absorption across the 400–1000 Hz range. Notably, this structure also exhibits the rainbow trapping effect. For its design, an effective medium approach (EMA) is combined with the Genetic Algorithm optimization, i.e., a homogenization-aided optimization framework is developed. Importantly, visco-thermal losses in the slits are rigorously modelled using the Stinson's model[45] in both of our theoretical and numerical models, rather than simplified loss-factor approximations seen in some of the previously studies on alternative structures. The accuracy of this homogenization scheme has been validated in our prior work. To the best of the authors' knowledge, the simultaneous realization of broadband perfect absorption and rainbow trapping using an MSSC structure has not been reported in the existing literature. Also, noteworthily, the proposed MSSC array is amenable to integration within a waveguide without requiring additional boundary treatments, while also maintaining the potential for ventilation.

Each MSSC element of, as depicted in Fig. 1, is characterized by its outer radius $r_{o,n}$, inner radius $r_{i,n}$, thickness h_n, slit width d_n, and number of slits N_n, where the subscript n denotes the index of each element. Through homogenization, the square unit cell (with lattice constant L) embedding the MSSC element is equivalently defined by an effective wavenumber k_{eff} and normalized characteristic impedance z_{eff}, both of which are dependent on the element's geometrical parameters. This framework allows the frequency-dependent transmission $T(f)$, reflection $R(f)$, and absorption $\alpha(f)$ coefficients of the metamaterial to be expressed in terms of the effective parameters, enabling efficient topology optimization to be conducted.

The optimization intervals for the geometrical parameters are set as: [16 mm, 35 mm] ($r_{o,n}$), [1 mm, 8 mm] (h_n), [0.1 mm, 1 mm] (d_n), and [2,4] (N_n), targeting for absorption maximization within the designated frequency range. It should be noted that N_n is enforced with an integer constraint, and the remaining parameters are treated as continuous variables within their respective bounds.

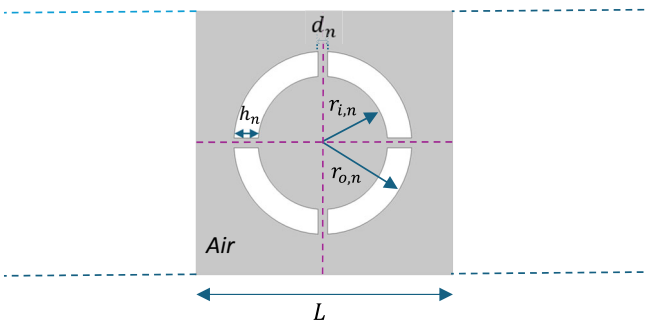

Fig. 1 | Schematic illustration of a 4-slit MSSC element. The grey region represents the surrounding air as the background medium.

Results

Single-frequency perfect absorption

We commence our analysis by investigating single-frequency perfect absorption (SFPA) at 500 Hz, achieved through a topologically optimized MSSC array consisting of 2 elements. The associated geometrical parameters are presented in Table 1, and the configuration is illustrated in Fig. 2. Particularly, the resonance frequencies of the individual elements predicted

Table 1 | Geometrical parameters of the SFPA-optimized MSSC array consisting of 2 elements, including the predicted resonance frequencies ($Re(f_{res,lossy,n})$) from Eq. (29) (*Analytical*) and FEM (*Numerical*)

n	$r_{o,n}$ (*mm*)	$r_{i,n}$ (*mm*)	h_n (*mm*)	d_n (*mm*)	N_n	$Re(f_{res,lossy,n})$ (*Hz*) (*Analytical*)	$Re(f_{res,lossy,n})$ (*Hz*) (*Numerical*)
1	32.8	30.5	2.3	0.4	3	540	544
2	35.0	29.1	5.9	0.9	2	458	466

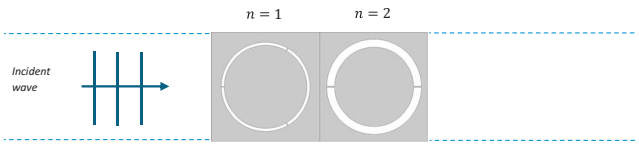

Fig. 2 | Geometry of the SFPA-optimized MSSC array.

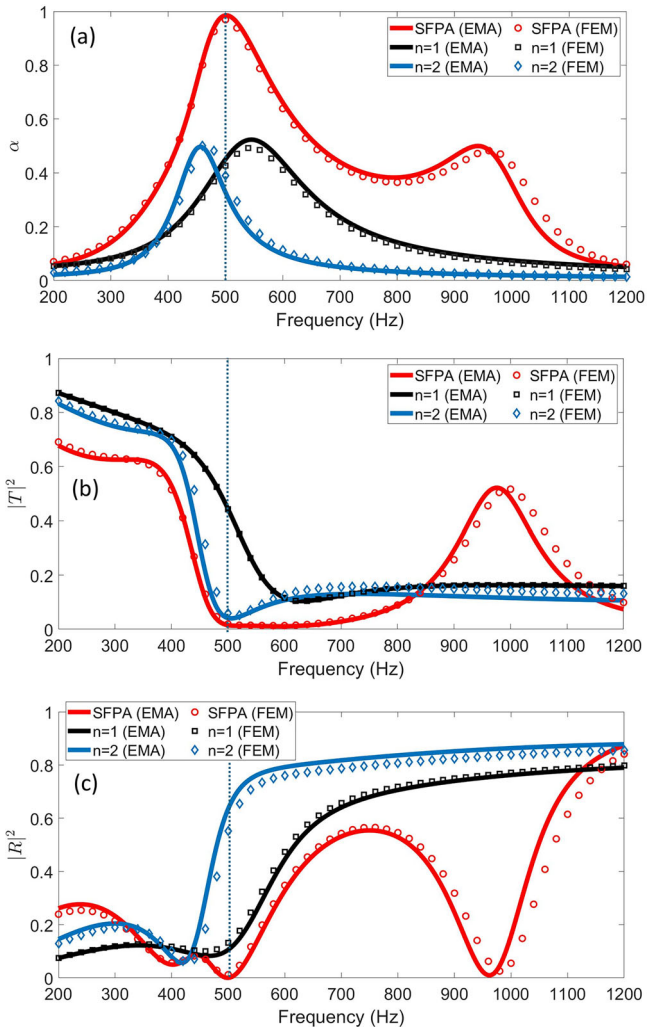

Fig. 3 | The SFPA-optimized MSSC array and the individual elements ($n = 1$ and $n = 2$). Analytical (*EMA*) and numerical (*FEM*) (**a**) absorption, (**b**) transmission, and (**c**) reflection coefficients. The dotted lines mark the target frequency of 500 Hz for reference.

using Eq. (29) (the real part) are also compared with the peak frequencies extracted from the FEM absorption coefficient curves. The negligible discrepancies between analytical and numerical values highlight the remarkable accuracy of our derived prediction formula, with visco-thermal losses rigorously taken into account.

Figure 3 presents both the analytical (Eqs. (1–3)) and numerical (FEM) absorption, transmission, and reflection coefficients of the optimized MSSC array, as well as for the individual elements ($n = 1$ and $n = 2$). Excellent agreement is observed between the results. Notably, the dips in transmission and reflection, along with the peak in absorption, are perfectly collocated at the target frequency of 500 Hz in both methods. Significantly, at this frequency, the absorption coefficients attain near-unity values - 0.99 (analytical) and 0.98 (numerical) - indicating the establishment of a near-perfect absorption condition and the realization of quasi-critical coupling in this metamaterial composed of MSSC elements $n = 1$ and $n = 2$. Remarkably, this sub-wavelength structure has a total length of merely 14.8 cm – almost 4.7 times shorter than the corresponding wavelength.

Notably, single-frequency perfect absorption is not achieved at the resonance frequencies of individual elements when considered in isolation. A considerable amount of reflection and transmission remains at these frequencies. This limitation arises primarily from two factors: (i) the narrow intrinsic resonance bandwidth of individual elements, which restricts full energy absorption at resonance, and (ii) the lack of sufficient interaction between the individual elements to satisfy the critical coupling condition, where visco-thermal losses precisely balance energy leakage at resonance. However, by assembling these elements into a strategically optimized MSSC array, these constraints are effectively mitigated, enabling single-frequency perfect/near-perfect absorption.

To demonstrate the occurrence of quasi-critical coupling in this optimized structure at 500 Hz, the normalized effective impedance z_{eff}/z_0 is plotted in Fig. 4a, b. Clearly, at this frequency, the normalized effective resistance (the real part of z_{eff}/z_0) is very close to unity, indicating excellent impedance matching between the MSSC array and the surrounding medium (air). Simultaneously, the reactance (the imaginary part of z_{eff}/z_0) is almost zero, attaining a value of just –0.02, suggesting that the intrinsic losses are effectively balanced – an essential condition for achieving quasi-critical coupling.

In contrast, as shown in Fig. 4c, d, the individual element $n = 1$ exhibits a normalized effective resistance of 1.14 at 500 Hz, while its normalized reactance remains significantly non-zero, reaching approximately –0.48. Moreover, although unit resistance is observed at its own resonance frequency, the reactance does not vanish, indicating that while the matching of resistance with air is achieved, the intrinsic losses remain uncompensated. The situation is even less favourable for the element $n = 2$, as illustrated in Fig. 4e, f, where neither the normalized resistance nor reactance approaches unity or zero – at 500 Hz or at its own resonance frequency. These results thus demonstrate that, for a single element, fundamental impedance mismatch with the surrounding medium is inevitable at resonance, and the absence of sufficient coupling prevents the balance between intrinsic losses and energy leakage. Consequently, as previously discussed, the absorption coefficient remains well below unity, and coherent absorption cannot be achieved.

Meanwhile, the asymmetric nature of the absorption characteristics exhibited by this optimized MSSC array warrants further discussion. As illustrated in Fig. 5a, b, by reversing the order of the constituent elements and allowing the incident wave to first impinge upon the element $n = 2$ with the lower resonance frequency, a markedly different response is observed. The absorption peak shifts leftward to 443 Hz, while the absorption coefficient severely drops to merely 0.64, failing to achieve single-frequency perfect absorption at

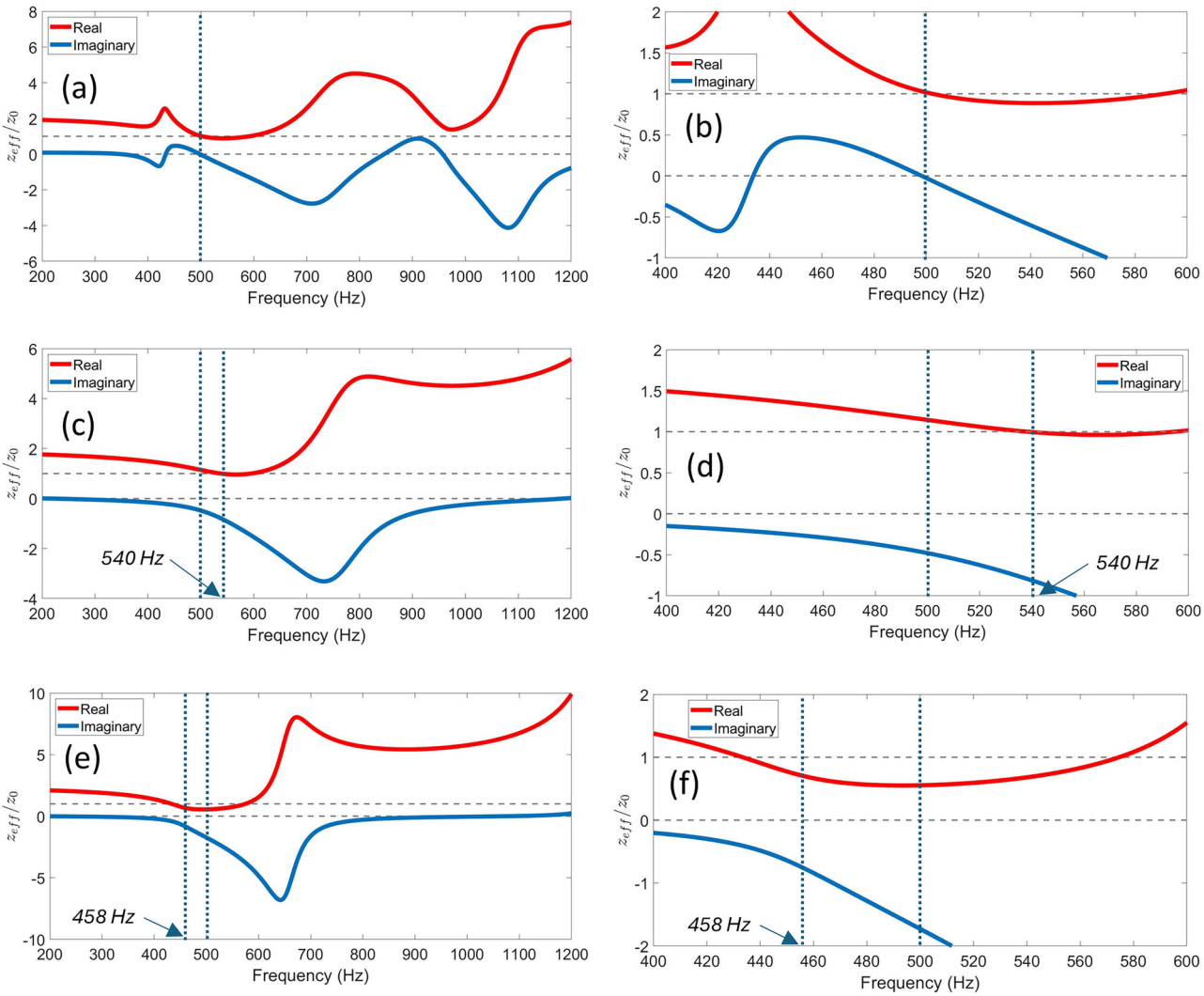

Fig. 4 | Real and imaginary parts of the normalized effective impedance z_{eff}/z_0. **a** The SFPA-optimized MSSC array, (**c**) the element $n = 1$, and (**e**) the element $n = 2$. Panels (**b**), (**d**), and (**f**) show zoomed-in views of panels (**a**), (**c**), and (**e**), respectively, over the frequency range [400, 600] Hz. The dotted lines mark the target frequency of 500 Hz and the resonance frequency of each element for reference.

both 443 Hz and 500 Hz. Additionally, significantly stronger reflection arises between 450 Hz and 1200 Hz, whereas transmission remains largely unaffected throughout the spectrum. A careful investigation into the effective impedance for this reversed structure, shown in Fig. 5c, d, reveals that the near-perfect impedance matching previously achieved is disrupted. The inherent losses are no longer sufficiently compensated, as evidenced by the absence of any frequency exhibiting both unit normalized resistance and zero reactance. These findings confirm that the critical coupling condition necessary for perfect absorption is lost when the structure is reversed, highlighting the pronounced asymmetry in both absorption and impedance behaviour inherent to this metamaterial design.

Additionally, a notable physical characteristic of the optimized structure is its graded distribution in both the outer radius r_o and the resonance frequencies of the individual elements. Through the optimization process, the smallest element – corresponding to the highest resonance frequency – is automatically positioned at the front of the structure. This arrangement contributes significantly to enhancing impedance matching within the metamaterial. As will be discussed in the next subsection, this graded configuration also plays a crucial role in achieving perfect absorption over a broader frequency range and enables the realization of the rainbow trapping phenomenon using a larger array of elements.

Broadband perfect absorption

By incorporating a greater number of MSSC elements and allowing interaction among their resonance behaviours across a wider frequency spectrum through the proposed optimization framework, the critical coupling condition can be satisfied in an extended metamaterial configuration,ultimately enabling the realization of broadband perfect absorption (BBPA).

In this subsection, a structure consisting of 8 elements is optimized to achieve broadband perfect absorption over the low-frequency range of [400, 1000] Hz. The optimized geometrical parameters are presented in Table 2, and the corresponding structure is illustrated in Fig. 6. The analytical and numerical resonance frequencies of each element are also included in the table to demonstrate their distribution. Again, as anticipated, only negligible discrepancies are observed between the analytical and numerical predictions. Furthermore, the feature of graded distribution in both the outer radius r_o and the resonance frequencies is preserved in this broadband-optimized structure.

The analytical and numerical transmission, reflection, and absorption coefficients of this optimized structure are plotted in Fig. 7a. Once again, excellent agreement is observed between the two approaches. Within the designated frequency range of 400–1000 Hz, the absorption coefficient exhibits an almost-flat curve close to unity, while both the transmission and

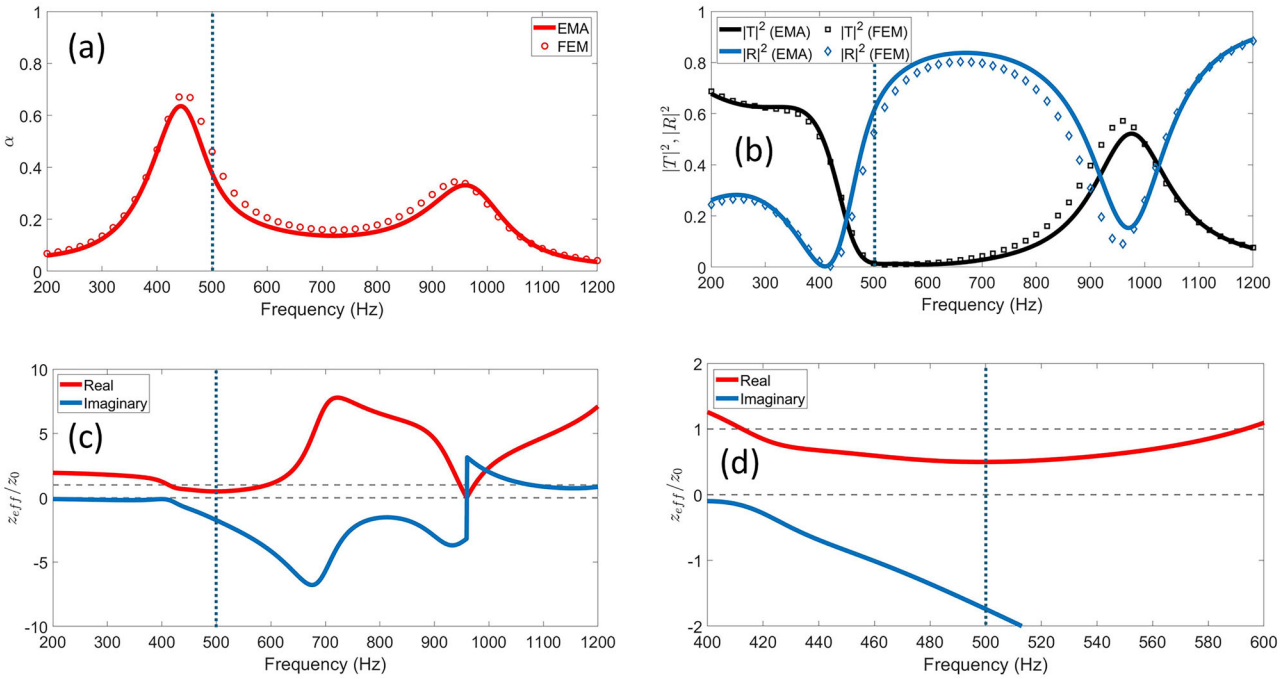

Fig. 5 | The reversed SFPA-optimized MSSC array. Analytical (*EMA*) and numerical (*FEM*) (**a**) absorption, (**b**) transmission, and reflection coefficients; (**c**) Real and imaginary parts of the normalized effective impedance z_{eff}/z_0; (**d**) Zoomed-in view of panel (**c**) over the frequency range [400, 600] Hz. The dotted lines mark the target frequency of 500 Hz for reference.

Table 2 | Geometrical parameters of the BBPA-optimized MSSC array consisting of 8 elements, including the predicted resonance frequencies $Re(f_{res,lossy,n})$ from Eq. (29) (*Analytical*) and FEM (*Numerical*)

n	$r_{o,n}$ (*mm*)	$r_{i,n}$ (*mm*)	h_n (*mm*)	d_n (*mm*)	N_n	$Re(f_{res,lossy,n})$ (*Hz*) (*Analytical*)	$Re(f_{res,lossy,n})$ (*Hz*) (*Numerical*)
1	18.3	15.7	2.6	0.3	3	926	938
2	24.8	21.2	3.6	0.5	4	877	879
3	26.5	25.0	1.5	0.3	4	862	863
4	27.6	24.7	2.9	0.4	4	741	743
5	29.0	26.8	2.2	0.3	4	648	662
6	33.0	31.2	1.8	0.3	3	496	509
7	34.0	30.4	3.6	0.4	2	393	402
8	35.0	31.9	3.1	0.3	3	375	400

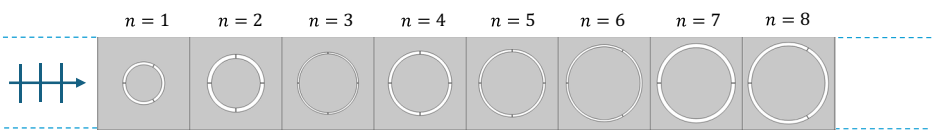

Fig. 6 | Geometry of the BBPA-optimized MSSC array.

reflection coefficient curves stay very close to zero, clearly indicating the achievement of near-perfect absorption across this interval. Impressively, the averaged absorption coefficient over this frequency range is 0.99. Notably, this remarkable high-performance absorption across a 600 Hz bandwidth is achieved using a compact, sub-wavelength structure measuring only 45.6 cm in length - approximately half the wavelength at 400 Hz. Also, with the individual absorption coefficients of each MSSC element depicted in Fig. 7b, it is reaffirmed that achieving perfect absorption with a single element alone is infeasible, and the importance of inter-element interaction is further emphasized.

As illustrated in Fig. 8a and b, analysis of the normalized effective impedance of the BBPA-optimized MSSC array reveals that, between 400 Hz and 1000 Hz, the normalized resistance and reactance remain consistently close to unity and zero, respectively. This confirms that the optimized structure achieves exceptional impedance matching with air across a much broader frequency range, enabling broadband quasi-critical coupling. As a result, both transmission and reflection are effectively suppressed within this range. However, outside the designated frequency range, the normalized resistance and reactance respectively start deviating significantly from unity and zero, leading to emerging substantial transmission and reflection, as seen in Fig. 7a.

Furthermore, similar to the SFPA-optimized MSSC array, this BBPA-optimized MSSC array also exhibits pronounced asymmetry. Its impedance characteristics and acoustic response become markedly altered when the structure is reversed. The broadband impedance matching, critical coupling, and perfect absorption are no longer preserved, as demonstrated by the normalized effective impedance in Fig. 8c and the absorption, transmission, and reflection coefficients in Fig. 9a and b. Notably, reversing the structure increases the reflectance substantially, while transmission remains unaffected.

A point of particular interest regarding this broadband optimized structure is its ability to also manifest the renowned rainbow trapping phenomenon. Attributed to its inherent graded geometrical profile and the cascading sequence of resonance frequencies of its elements, as depicted in Table 2, this structure is capable of predominantly localizing acoustic energy near these resonance frequencies in descending order. However, it should be reminded that due to the interacting effect between elements, some localization frequencies are shifted slightly. The actual frequencies at which the localization occurs are observed to be [300, 353, 435, 535, 650, 775, 780, 895] Hz. With the FEM-simulated pressure fields at these frequencies presented in Fig. 10, the rainbow trapping effect and the dominant energy localization at each successive frequency is apparent. Utilizing this structure, simultaneous broadband perfect absorption and energy harvesting near each of the resonance frequencies becomes feasible.

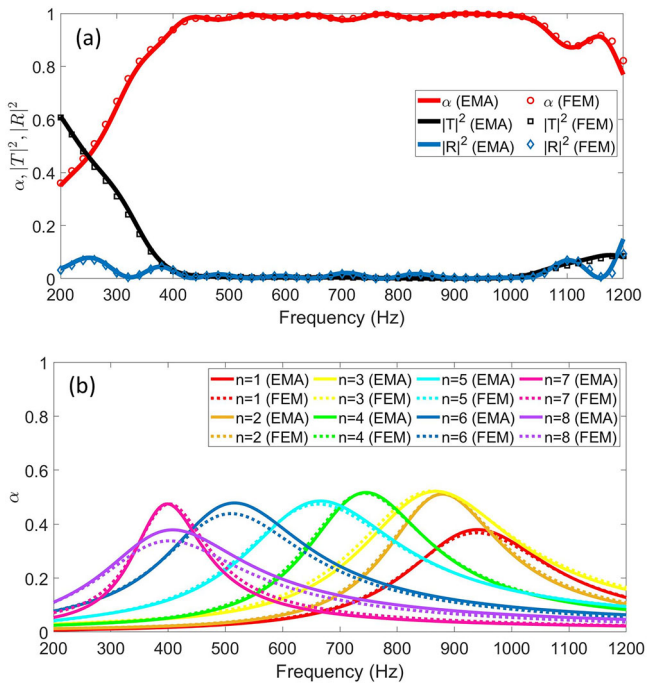

Fig. 7 | The BBPA-optimized MSSC array. Analytical (*EMA*) and numerical (*FEM*) (**a**) absorption, transmission, and reflection coefficients. **b** Absorption coefficients of individual elements ($n = 1$ to 8).

Discussion

In this work, we present two metamaterial structures composed of sub-wavelength multi-slit sonic crystal (MSSC) elements, optimally engineered to achieve exceptional acoustic performance: single-frequency perfect absorption at 500 Hz and broadband perfect absorption over the range of 400–1000 Hz, using arrays of 2 and 8 elements, respectively, in a transmission setting. The topology optimization of these MSSC-based metamaterials is conducted by combining a Genetic Algorithm with a proposed effective medium homogenization scheme. Crucially, this homogenization model accounts for visco-thermal losses inherent to the slit regions, thereby making the theoretical framework more comprehensive and robustness in predicting the lossy behavior of the elements and thus the array, and further enhancing the reliability of the illustrated homogenization-aided optimization methodology.

The excellent agreement between analytical predictions and numerical simulations validates the accuracy of the proposed theory and confirms the feasibility of achieving perfect absorption using very simple and compact structures through strategic topology design. Notably, due to the intrinsic sub-wavelength resonance characteristics of the elements, the total lengths

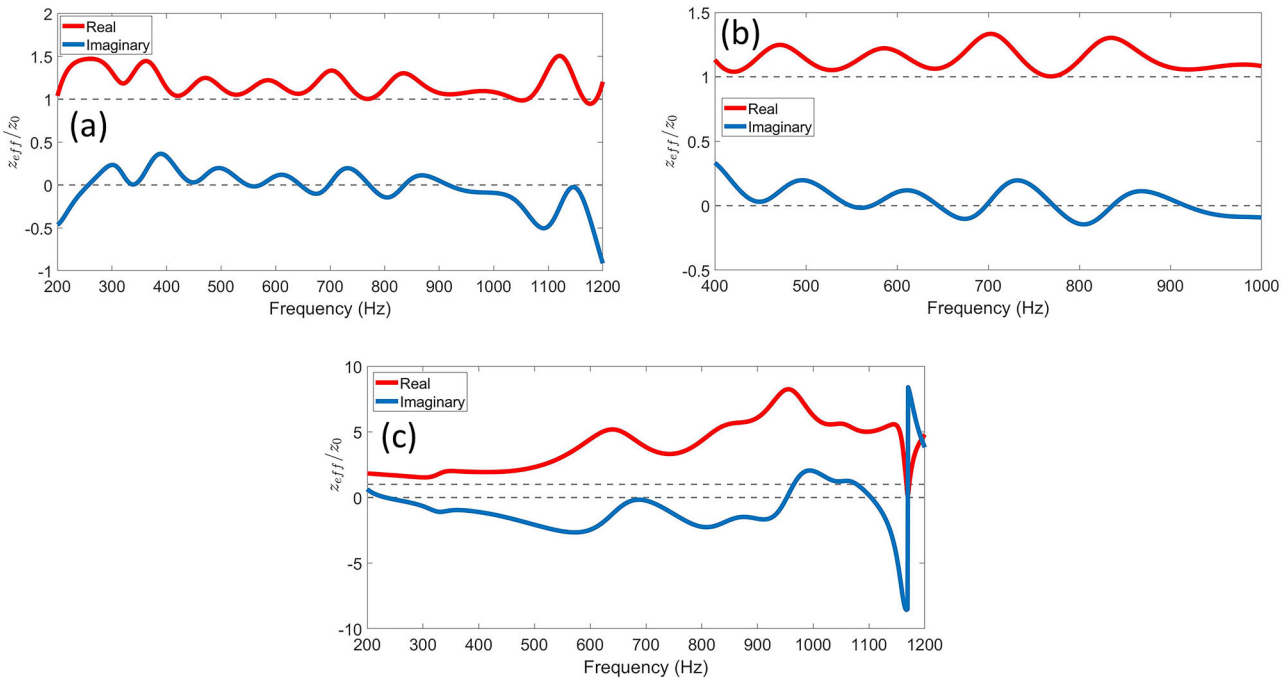

Fig. 8 | Real and imaginary parts of the normalized effective impedance z_{eff}/z_0. **a** The BBPA-optimized MSSC array, and (**c**) the reversed BBPA-optimized MSSC array. **b** Zoomed-in view of panel (**a**) over the frequency range [400, 1000].

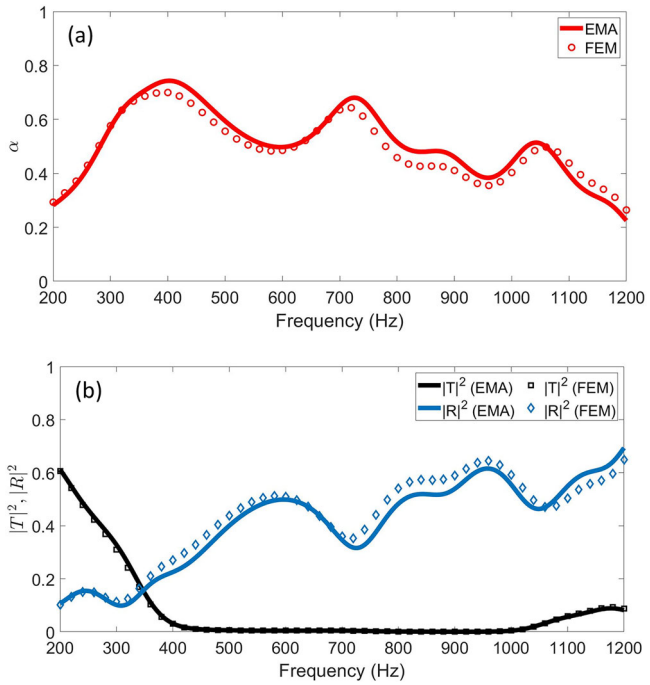

Fig. 9 | The reversed BBPA-optimized MSSC array. Analytical (*EMA*) and numerical (*FEM*) (**a**) absorption, (**b**) transmission, and reflection coefficients.

of the optimized structures are significantly reduced – approximately 6 and 2 times shorter than the wavelength at 400 Hz for the single-frequency and broadband configurations, respectively. While the size reduction in the design of broadband perfect absorption is relatively modest, its ability to sustain high absorption over a wide 600 Hz bandwidth remains a remarkable feature, underscoring its strong potential for practical applications. Additionally, both optimized metamaterial configurations exhibit a graded profile, with the size of each element increasing along the array and the corresponding resonance frequency decreasing – a characteristic similarly observed in previous studies in refs. 18,29,30 in connection with achieving perfect absorption and the rainbow trapping effect.

Furthermore, both the single-frequency and broadband configurations exhibit quasi-perfect impedance matching with the surrounding medium, accompanied by quasi-critical coupling between energy leakage and internal losses. This results in vanishing transmission and reflection within their respective target frequency ranges. These structures also display pronounced asymmetry: when the direction of wave incidence is reversed, the optimized impedance matching and critical coupling conditions break down, leading to significant deterioration of absorption performance, highlighting the importance of structural orientation in the design of high-efficiency acoustic metamaterials.

Thanks to the frequency-cascade property of the MSSC array optimized for broadband perfect absorption, the rainbow trapping effect is realized, wherein acoustic energy is progressively confined within the elements - from high to low frequencies. This demonstrates that rainbow trapping is not exclusive to complex architectures such as sawtooth arrays, coiling-up space designs, side-branch Helmholtz resonators, or graded grooves shown in previous studies, instead it can be effectively achieved with this compact and structurally simple MSSC-based metamaterial.

In summary, we demonstrate that carefully engineered MSSC arrays can achieve both single-frequency and broadband perfect absorption through an efficient homogenization-assisted topology optimization approach. Compared to conventional FEM-based optimization methods, our framework offers a much more cost-effective and attractive alternative for navigating unmanageably large parameter spaces, without compromising accuracy. The proposed optimization strategy and the MSSC-based designs reported herein are expected to contribute valuable insights to future research in acoustic energy harvesting, cloaking, and confinement. In particular, the strong low-frequency absorption capabilities make these structures promising candidates for practical noise mitigation applications, such as in plenum windows, ducts, and building materials.

Looking ahead, integrating MSSC-based metamaterials with complementary components – such as porous materials, meta-membranes, or coiled-up structures – may pave the way for more sophisticated and versatile acoustic control solutions. Furthermore, inspired by the work of Davies et al.[46], future research would carefully examine the sensitivity of material properties and effective parameters, as well as the formulation of objective functions, to ensure robust and physically meaningful optimization outcomes across diverse physical scenarios.

Methods

Theoretical Model: Effective Medium Approach

Consider a normally incident plane wave given by $p_i = e^{ikx}$, where $i = \sqrt{-1}$, $k = \omega/c$ is the ambient wavenumber, ω the angular frequency, and c the ambient sound speed in air. A rigid multi-slit sonic crystal (MSSC) element is characterised by the outer radius r_o, inner radius r_i, thickness h, slit width d, and slit number N, and is embedded within a square unit cell with lattice constant L. In the frequency regime where $kL < 2\pi$, the transmission T, reflection R, and absorption α coefficients of the MSSC element within a rigid waveguide can be analytically expressed as[47,48]

$$T = \left(1 + \frac{2}{kL}\sum_{n=-\infty}^{\infty} A_n\right)e^{ikL}, \tag{1}$$

$$R = \left(\frac{2}{kL}\sum_{n=-\infty}^{\infty} (-1)^n A_n\right)e^{ikL}, \tag{2}$$

$$\alpha = 1 - |T|^2 - |R|^2. \tag{3}$$

If no visco-thermal losses are accounted for, the equality $|T|^2 + |R|^2 = 1$ holds. In the regime $kr_o < 2$, it is adequate to consider only A_n corresponding to $n \in [-3,\ 3]$[49]:

$$A_0 = z_0 \frac{1 - z_2(\mathcal{H}_0 + \mathcal{H}_4 - 2\mathcal{H}_2)}{(1 - z_0\mathcal{H}_0)\left[1 - z_2(\mathcal{H}_0 + \mathcal{H}_4)\right] - 2z_0 z_2 \mathcal{H}_2^2}, \tag{4}$$

$$A_1 = z_1 \frac{1 - z_3(\mathcal{H}_0 + \mathcal{H}_6 - \mathcal{H}_2 - \mathcal{H}_4)}{\left[1 - z_1(\mathcal{H}_0 + \mathcal{H}_2)\right]\left[1 - z_3(\mathcal{H}_0 + \mathcal{H}_6)\right] - z_1 z_3 (\mathcal{H}_2 + \mathcal{H}_4)^2}, \tag{5}$$

$$A_2 = z_2 \frac{1 - z_0(\mathcal{H}_0 - \mathcal{H}_2)}{(1 - z_0\mathcal{H}_0)\left[1 - z_2(\mathcal{H}_0 + \mathcal{H}_4)\right] - 2z_0 z_2 \mathcal{H}_2^2}, \tag{6}$$

$$A_3 = z_3 \frac{1 - z_1(\mathcal{H}_0 - \mathcal{H}_4)}{\left[1 - z_1(\mathcal{H}_0 + \mathcal{H}_2)\right]\left[1 - z_3(\mathcal{H}_0 + \mathcal{H}_6)\right] - z_1 z_3 (\mathcal{H}_2 + \mathcal{H}_4)^2}, \tag{7}$$

in which $\mathcal{H}_0$ to $\mathcal{H}_6$ are given in ref. 49 for the low-frequency regime, considering only one propagating mode, as

$$\mathcal{H}_0 = \frac{1}{\pi\delta} - 1 - \frac{2i}{\pi}\left[\ln\left(\frac{\beta\delta}{2}\right) + \sum_{\mathrm{q}=1}^{\infty}\left(\frac{1}{\sqrt{\mathrm{q}^2 - \delta^2}} - \frac{1}{\mathrm{q}}\right)\right], \tag{8}$$

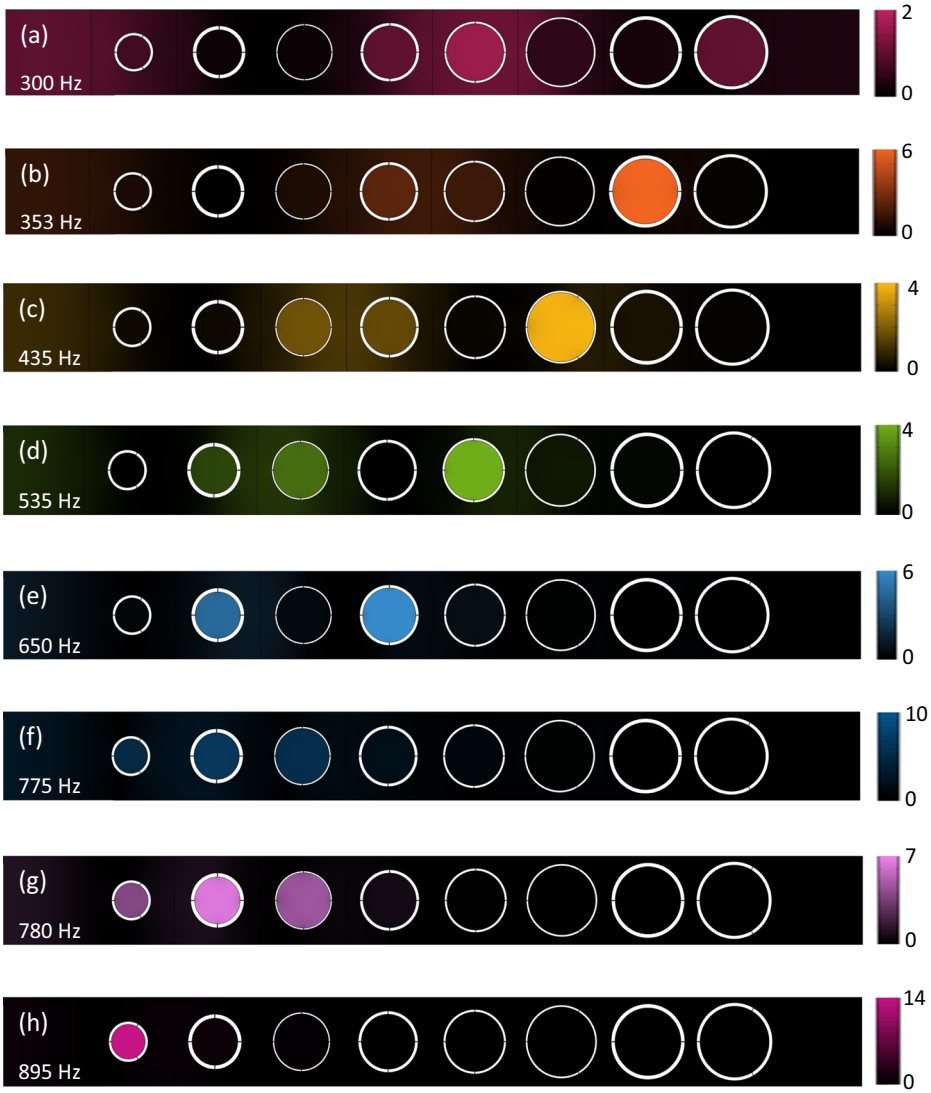

Fig. 10 | FEM-simulated pressure fields of the BBPA-optimized MSSC array. At (**a**) 300 Hz, (**b**) 353 Hz, (**c**) 435 Hz, (**d**) 535 Hz, (**e**) 650 Hz, (**f**) 775 Hz, (**g**) 780 Hz, (**h**) 895 Hz. The colour scale represents $|P/P_0|^2$, where $P_0 = 1$ Pa.

$$\mathcal{H}_{2n} = \frac{1}{\pi\delta} + \frac{i}{\pi}\left[\frac{1}{n} + \sum_{q=1}^{n}\frac{(-4)^q(n+q-1)!B_{2q}}{(2q)!(n-q)!\delta^{2q}} - \frac{2(-1)^n}{\pi\delta^{2n}}\sum_{q=1}^{\infty}\frac{\left[q-\sqrt{q^2-\delta^2}\right]^{2n}}{\sqrt{q^2-\delta^2}}\right], \tag{9}$$

where $\delta = kL/2\pi$, $\beta \approx 1.718$, B_{2n}'s are the Bernoulli numbers, $n = 1, 2, 3$.

In Eqs. (4–7), the scattering coefficient z_n of the MSSC element, considering visco-thermal losses in the slits, is[50]

$$z_n = -\frac{\rho_l W_1 W_3 J_n'(kr_o) - \rho J_n(kr_o)\left[W_1 J_n'(k_l r_o) + W_2 Y_n'(k_l r_o)\right]}{\rho_l W_1 W_3 H_n'(kr_o) - \rho H_n(kr_o)\left[W_1 J_n'(k_l r_o) + W_2 Y_n'(k_l r_o)\right]}, \tag{10}$$

where J, Y, H denote the Bessel function of first, second kind, and Hankel function of the first kind, respectively. The prime notation indicates differentiation performed with respect to the radial argument, ρ is the ambient density of air, and details of W_1, W_2, and W_3 can be found in ref. 50. The effective fluid parameters k_l and ρ_l, of the MSSC element, are derived as

$$k_l = k_{slit}\sqrt{1 + \frac{2\Delta}{h}\cdot\frac{\rho}{\rho_{slit}}}, \tag{11}$$

$$\rho_l = \frac{1}{\mathcal{F}}\left(\rho_{slit} + \frac{2\Delta}{h}\rho\right), \tag{12}$$

where[51]

$$\mathcal{F} = \frac{Nd}{2\pi r_{eff}}, \tag{13}$$

$$r_{eff} = \frac{r_i + r_o}{2}, \tag{14}$$

$$\Delta = \frac{d}{\mathcal{F}^2\pi^3}\sum_{n=1}^{\infty}\frac{sin^2(n\pi\mathcal{F})}{n^3}. \tag{15}$$

$\mathcal{F}$, r_{eff}, and Δ are respectively the filling fraction of the slits, the effective radius of the resonator, and the end-correction term accounting for the effect near the slits. More derivation details for

Table 3 | Physical parameters and their values

Physical Parameters	Values [unit]
Sound speed in air (c)	343 $[m/s]$
Density of air (ρ)	1.204 $[kg/m^3]$
Dynamic viscosity of air (η)	1.825×10^{-5} $[Pa \cdot s]$
Specific heat ratio of air (γ)	1.4
Prandtl number of air (Pr)	7.309×10^{-1}
Thermal conductivity of air (k_{th})	2.514×10^{-2} $[W/(m \cdot K)]$
Heat capacity at constant pressure (C_p)	1.007×10^{3} $[J/(kg \cdot K)]$

Eqs. (11) and (12), and the physical interpretation of the latter, can be found in *Supplementary Information*. The parameters ρ_{slit}, c_{slit}, and k_{slit} are correspondingly the complex frequency-dependent effective density of air, sound speed, and wavenumber, within the slit, accounting for visco-thermal losses and are defined through the Stinson's model[45],

$$\rho_{slit} = \rho\left[1 - \frac{\tanh\left(G_\rho\right)}{G_\rho}\right]^{-1}, \tag{16}$$

$$K_{slit} = K\left[1 + (\gamma - 1)\frac{\tanh\left(G_K\right)}{G_K}\right]^{-1}, \tag{17}$$

as $c_{slit} = \sqrt{K_{slit}/\rho_{slit}}$, $k_{slit} = \omega/c_{slit}$. In Eqs. (16), (17), $K = \rho c^2$ is the ambient bulk modulus of air, $G_\rho = (d/2)\sqrt{-i\omega\rho/\eta}$, and $G_K = (d/2)\sqrt{-i\omega\rho\,\mathrm{Pr}/\eta}$, where γ, η, and Pr signify the specific heat ratio, dynamic viscosity, and Prandtl number of air, respectively. The values used for these physical parameters are listed in Table 3 in below. It is also reminded that ρ_{slit}, c_{slit}, and k_{slit} are functions of ω and d, with the involved physical parameters being constant.

The effective wavenumber k_{eff} and normalized characteristic impedance z_{eff} of the unit cell can thus be retrieved via a standard method outlined in ref. 52 as

$$z_{eff} = \frac{\mathcal{R}}{(1-R)^2 - T^2}, \tag{18}$$

$$k_{eff} = \frac{-i}{L}\cdot\ln\left(\frac{1 + T^2 - R^2 - \mathcal{R}}{2T}\right), \tag{19}$$

where $\mathcal{R} = \pm\sqrt{(R^2 - T^2 - 1)^2 - 4T^2}$ and the sign is determined by the condition $\mathrm{Re}\left(z_{\mathrm{eff}}\right) \geq 0$. The effective density ρ_{eff} and sound speed c_{eff} follow as

$$\rho_{eff} = z_{eff}k_{eff}\rho/k, \tag{20}$$

$$c_{eff} = \omega/k_{eff}. \tag{21}$$

The frequency-dependent transmission T_{N_l}, reflection R_{N_l}, and absorption α_{N_l} coefficients across a N_l-layer structure of effective media (equivalently, an array of MSSC elements in our case) each defined by its own parameters $z_{eff,j}$ and $k_{eff,j}$, and thickness L, where $j = 1, 2, \ldots, N_l$ denotes the indexing of each layer, can be calculated based on a recurring approach[53]

$$T_{N_l} = \prod_{q=0}^{N_l}\frac{\left[Z_{in}^{(q)} + Z_q\right]e^{i\phi_q}}{Z_{in}^{(q)} + Z_{q+1}}, \tag{22}$$

$$R_{N_l} = \frac{Z_{in}^{(1)} - Z_0}{Z_{in}^{(1)} + Z_0}, \tag{23}$$

$$\alpha_{N_l} = 1 - \left|T_{N_l}\right|^2 - \left|R_{N_l}\right|^2, \tag{24}$$

where

$$\phi_p = \begin{cases} 0, & p = 0 \\ k_{eff,p}L, & p = 1, 2, \ldots, N_l \end{cases}, \tag{25}$$

$$Z_{in}^{(p)} = \begin{cases} z & , p = 0, N_l + 1 \\ \left[\left(Z_{in}^{(p+1)} - iZ_p\tan\left(k_{eff,p}L\right)\right)/\left(Z_p - iZ_{in}^{(p+1)}\tan\left(k_{eff,p}L\right)\right)\right]Z_p & , p = 1, 2, \ldots, N_l \end{cases}, \tag{26}$$

$$Z_p = \begin{cases} z & , p = 0, N_l + 1 \\ z_{eff,p} & , p = 1, 2, \ldots, N_l \end{cases}, \tag{27}$$

and $z = \rho c$ is the characteristic impedance of air. Therefore, based on Eqs. (22–27), topology optimization of MSSC array can be performed.

Regarding the Genetic Algorithm for optimization, targeting maximum absorption over the frequency range $[f_L, f_U]$ with a resolution of 1 Hz, the optimal geometrical parameter set of the MSSC array is the argument of the maximized multivariate objective function F_{obj}

$$F_{obj} = \sum_{f=f_L}^{f_U}\alpha_{N_l}(f). \tag{28}$$

The values used for the population size, crossover rate, objective function tolerance, and constraint tolerance in the algorithm are 100, 0.8, 10^{-8}, and 10^{-8}, respectively.

Besides, the resonance frequency $f_{R,lossy}$ of MSSC element considering visco-thermal effects can be estimated by our derived prediction formula

$$f_{R,lossy} = \Lambda \cdot f_{R,lossless} \tag{29}$$

where

$$\Lambda = \sqrt{\frac{\rho}{\hat{\rho}_{slit}}\cdot\frac{h + 2\Delta}{h + 2\Delta\cdot\frac{\rho}{\hat{\rho}_{slit}}}}, \text{ and} \tag{30}$$

$$f_{R,lossless} = \frac{c}{2\pi}\sqrt{\frac{2Ndh}{\pi r_i^2\left(r_o + r_i\right)\left(h + \frac{2\Delta}{1+\mathcal{F}^2}\right)\ln\left(\frac{r_o}{r_i}\right)}}. \tag{31}$$

Noteworthily, Eq. (31) is the resonance frequency of MSSC element in the lossless case. Here, $\hat{\rho}_{slit} = \rho_{slit}(\omega_{res})$, with $\omega_{res} = 2\pi f_{R,lossless}$. It is important to note that Eq. (29) establishes the lossless-lossy relationship between the resonance frequency without and with visco-thermal losses accounted for. Besides, Eq. (29) will simply reduce to Eq. (31) if $\hat{\rho}_{slit} = \rho$, i.e., when visco-thermal losses are absent in the slits. Also, regarding the shift in resonance frequency when losses are considered, it should be noted that from Eq. (30) this shift is mainly attributed to the medium's viscosity.

Numerical Model: Finite Element Method

COMSOL Multiphysics 5.5™ based on the Finite Element Method (FEM) is used to validate the performance of the optimized MSSC array. The model height corresponds to the lattice constant $L = 0.08\,m$, and the length is $(N_l + 2)L\,m$. The background medium is set as air. Two ports are defined at the left and right ends of the model to generate a 1-Pa normally incident plane wave and to absorb the outgoing acoustic wave, respectively. All

boundaries except these ports are defined as rigid. No higher order acoustic modes arise within the model during the simulation. Visco-thermal losses within the slits are considered by specifically implementing the build-in '*Thermoviscous Acoustics*' module, which is based on the Low Reduced Frequency model[54]. For all other domains, the '*Pressure Acoustics*' module is applied. To capture also the coupling effects between these two modules, an '*Acoustic-Thermoviscous Acoustic Boundary*' condition is imposed at the openings and ends of each slit, i.e., at the interfaces between the modules. The frequency sweep covers 100 Hz to 1200 Hz with 1 Hz increments. Numerical transmission, reflection, and absorption coefficients are extracted directly using built-in commands.

For meshing, a frequency-dependent element sizing approach is adopted to reduce computational time by avoiding unnecessary refinements at lower frequencies, while maintaining at least 10 elements per wavelength throughout the target frequency range. To accurately capture the physics within the slits, a much finer mesh is applied there, with element sizes 5.5 to 6 times smaller than the slit width. This mesh density is determined through a convergence test, where the number of elements inside the slit is gradually increased until no further shift in the peak absorption frequency (numerical resonance frequency) is observed.

Data availability

Data available on request from the authors.

Code availability

Software *MATLAB* (version R2020b) and *COMSOL Multiphysics* (version 5.6) are used in this study. Code is available on request from the authors.

Received: 20 January 2025; Accepted: 23 August 2025;
Published online: 08 January 2026

References

1. Ma, G. C., Yang, M., Xiao, S. W., Yang, Z. Y. & Sheng, P. Acoustic metasurface with hybrid resonances. *Nat. Mater.* **13**, 873–878 (2014).
2. Mei, J. et al. Dark acoustic metamaterials as super absorbers for low-frequency sound. *Nat. Commun.* **3**, 756 (2012).
3. Cai, X. B., Guo, Q. Q., Hu, G. K. & Yang, J. Ultrathin low-frequency sound absorbing panels based on coplanar spiral tubes or coplanar Helmholtz resonators. *Appl. Phys. Lett.* **105**, 121901 (2014).
4. Chen, C. R., Du, Z. B., Hu, G. K. & Yang, J. A low-frequency sound absorbing material with subwavelength thickness. *Appl. Phys. Lett.* **110**, 221903 (2017).
5. Wang, Y., Zhao, H. G., Yang, H. B., Zhong, J. & Wen, J. H. A space-coiled acoustic metamaterial with tunable low-frequency sound absorption. *Epl.* **120**, 54001 (2017).
6. Wu, F. et al. Low-frequency sound absorption of hybrid absorber based on micro-perforated panel and coiled-up channels. *Appl. Phys. Lett.* **114**, 151901 (2019).
7. Groby, J. P., Huang, W., Lardeau, A. & Aurégan, Y. The use of slow waves to design simple sound absorbing materials. *J. Appl. Phys.* **117**, 124903 (2015).
8. Romero-García, V., Theocharis, G., Richoux, O. & Pagneux, V. Use of complex frequency plane to design broadband and sub-wavelength absorbers. *J. Acoust. Soc. Am.* **139**, 3394–3402 (2016).
9. Jiménez, N., Romero-Garcia, V., Pagneux, V. & Groby, J. P. Quasiperfect absorption by subwavelength acoustic panels in transmission using accumulation of resonances due to slow sound. *Phys. Rev. B.* **95**, 014205 (2017).
10. Long, H. Y., Cheng, Y. & Liu, X. J. Reconfigurable sound anomalous absorptions in transparent waveguide with modularized multi-order Helmholtz resonator. *Sci. Rep.* **8**, 15678 (2018).
11. Al Jahdali, R. & Wu, Y. Coupled Resonators for Sound Trapping and Absorption. *Sci. Rep.* **8**, 13855 (2018).
12. Ryoo, H. & Jeon, W. Dual-frequency sound-absorbing metasurface based on visco-thermal effects with frequency dependence. *J. Appl. Phys.* **123**, 11 (2018).
13. Duan, M., Yu, C., He, W., Xin, F. & Lu, T. J. Perfect sound absorption of Helmholtz resonators with embedded channels in petal shape. *J. Appl. Phys.* **130**, 13 (2021).
14. Li, J. F., Wang, W. Q., Xie, Y. B., Popa, B. I. & Cummer, S. A. A sound absorbing metasurface with coupled resonators. *Appl. Phys. Lett.* **109**, 9 (2016).
15. Li, Y. & Assouar, B. M. Acoustic metasurface-based perfect absorber with deep subwavelength thickness. *Appl. Phys. Lett.* **108**, 6 (2016).
16. Leroy, V. et al. Superabsorption of acoustic waves with bubble metascreens. *Phys. Rev. B.* **91**, 020301 (2015).
17. Wang, T., Wang, G. B., Zhang, R. J. & Ke, M. Z. Low-frequency underwater sound absorption metamaterial. *Phys. Scripta.* **97**, 125706 (2022).
18. Jiménez, N., Romero-García, V., Pagneux, V. & Groby, J. P. Rainbow-trapping absorbers: Broadband, perfect and asymmetric sound absorption by subwavelength panels for transmission problems. *Sci. Rep.* **7**, 13595 (2017).
19. Ryoo, H. & Jeon, W. Broadband sound absorption using multiple hybrid resonances of acoustic metasurfaces. *Int. J. Mech. Sci.* **229**, 107508 (2022).
20. Long, H. Y., Shao, C., Liu, C., Cheng, Y. & Liu, X. J. Broadband near-perfect absorption of low-frequency sound by subwavelength metasurface. *Appl. Phys. Lett.* **115**, 10 (2019).
21. Liu, C. R., Wu, J. H., Ma, F. Y., Chen, X. & Yang, Z. R. A thin multi-order Helmholtz metamaterial with perfect broadband acoustic absorption. *Appl. Phys. Express.* **2**, 084002 (2019).
22. Liu, C. R., Wu, J. H., Yang, Z. R. & Ma, F. Y. Ultra -broadband acoustic absorption of a thin microperforated panel metamaterial with multi-order resonance. *Compos. Struct.* **246**, 112366 (2020).
23. Gao, Y. X. et al. Broadband thin sound absorber based on hybrid labyrinthine metastructures with optimally designed parameters. *Sci. Rep.* **10**, 10705 (2020).
24. Qu, R. H., Guo, J. W., Fang, Y., Zhong, S. Y. & Zhang, X. Broadband acoustic meta-porous layer for reflected wave manipulation and absorption. *Int. J. Mech. Sci.* **227**, 107426 (2022).
25. Ni, X. et al. Acoustic rainbow trapping by coiling up space. *Sci. Rep.* **4**, 7038 (2014).
26. Zhou, C., Yuan, B. G., Cheng, Y. & Liu, X. J. Precise rainbow trapping for low-frequency acoustic waves with micro Mie resonance-based structures. *Appl. Phys. Lett.* **108**, 6 (2016).
27. Zhu, J. et al. Acoustic rainbow trapping. *Sci. Rep.* **3**, 1728 (2013).
28. Tsakmakidis, K. L., Boardman, A. D. & Hess, O. 'Trapped rainbow' storage of light in metamaterials. *Nature* **450**, 397–401 (2007).
29. Rosafalco, L., De Ponti, J. M., Iorio, L., Ardito, R. & Corigliano, A. Optimised graded metamaterials for mechanical energy confinement and amplification via reinforcement learning. *Eur. J. Mech. a-Solids.* **99**, 104947 (2023).
30. Wilks, B., Montiel, F. & Wakes, S. Rainbow reflection and broadband energy absorption of water waves by graded arrays of vertical barriers. *J. Fluid Mech.* **941**, A26 (2022).
31. Bell, A. A Resonance Approach to Cochlear Mechanics. *Plos One.* **7**, e47918 (2012).
32. Rupin, M., Lerosey, G., de Rosny, J. & Lemoult, F. Mimicking the cochlea with an active acoustic metamaterial. *N. J. Phys.* **21**, 093012 (2019).
33. Ammari, H. & Davies, B. Mimicking the active cochlea with a fluid-coupled array of subwavelength Hopf resonators. *Proc. Royal Soc. Math. Phys. Eng. Sci.* **476**, 20190870 (2020).

34. Marrocchio, R., Karlos, A. & Elliott, S. Waves in the cochlea and in acoustic rainbow sensors. *Wave Motion.* **106**, 102808 (2021).
35. Karlos, A. & Elliott, S. J. Cochlea-inspired design of an acoustic rainbow sensor with a smoothly varying frequency response. *Sci. Rep.* **10**, 10803 (2020).
36. Zhao, L. X. & Zhou, S. X. Compact acoustic rainbow trapping in a bioinspired spiral array of graded locally resonant metamaterials. *Sensors.* **19**, 788 (2019).
37. Chen, Z. S., Guo, B., Yang, Y. M. & Cheng, C. C. Metamaterials-based enhanced energy harvesting: A review. *Phys. B-Condens. Matter* **438**, 1–8 (2014).
38. Ao, X. Y. & Chan, C. T. Far-field image magnification for acoustic waves using anisotropic acoustic metamaterials. *Phys. Rev. E.* **77**, 025601 (2008).
39. Guenneau, S., Movchan, A., Petursson, G. & Ramakrishna, S. A. Acoustic metamaterials for sound focusing and confinement. *N. J. Phys.* **9**, 399 (2007).
40. Li, X. L., Lam, W. K. & Tang, S. K. Experimental investigation on the enhancement of plenum window noise reduction using solid scatterers. *J. Acoustical Soc. Am.* **153**, 1361–1374 (2023).
41. Tang, S. K. Narrow sidebranch arrays for low frequency duct noise control. *J. Acoust. Soc. Am.* **132**, 3086–3097 (2012).
42. Karthik, R., Barathula, S. & Srinivasan, K. Data-driven approach for prediction of band diagram of locally resonant sonic crystal. *J. Phys. D: Appl. Phys.* **57**, 135307 (2024).
43. Gurbuz, C., Kronowetter, F., Dietz, C., Eser, M. & Schmid, J. and S. Marburg, Generative adversarial networks for the design of acoustic metamaterialsa. *J. Acoust. Soc. Am.* **149**, 1162–1174 (2021).
44. Meng, H., Wen, J. H., Zhao, H. G. & Wen, X. S. Optimization of locally resonant acoustic metamaterials on underwater sound absorption characteristics. *J. Sound Vib.* **331**, 4406–4416 (2012).
45. Stinson, M. R. The Propagation of Plane Sound-Waves in Narrow and Wide Circular Tubes, and Generalization to Uniform Tubes of Arbitrary Cross-Sectional Shape. *J. Acoust. Soc. Am.* **89**, 550–558 (1991).
46. Davies, B., Fehertoi-Nagy, L. & Putley, H. J. On the problem of comparing graded metamaterials. *Proc. Royal Soc. A-Math. Phys. Eng. Sci.* **479**, 20230537 (2023).
47. Twersky, V. On scattering of waves by the infinite grating of circular cylinders. *IRE Trans. Antennas Propag.* **10**, 737–765 (1962).
48. Umnova, O., Krynkin, A., Chong, A. Y. B., Taherzadeh, S. & Attenborough, K. Comparisons of two effective medium approaches for predicting sound scattering by periodic arrays of elastic shells. *J. Acoust. Soc. Am.* **134**, 3619–3630 (2013).
49. Shenderov, E. Wave problems of underwater acoustics. Sudostroenie, Leningrad, **352**, 149 (1972).
50. Krynkin, A., Umnova, O., Chong, A. Y. B., Taherzadeh, S. & Attenborough, K. Scattering by coupled resonating elements in air. *J. Phys. D-App. Phys.* **44**, 125501 (2011).
51. Smits, J. & Kosten, C. *Sound absorption by slit resonators*. *Acta Acust. U. Acust.* **1**, 114–122 (1951).
52. Fokin, V., Ambati, M., Sun, C. & Zhang, X. Method for retrieving effective properties of locally resonant acoustic metamaterials. *Phys. Rev. B.* **76**, 144302 (2007).
53. Brekhovskikh, L. M. Waves in layered media. *Applied mathematicsand mechanics.* Vol. 561, 24 (New York, Academic Press, 1960).
54. Beltman, W. M. Viscothermal wave propagation including acousto-elastic interaction, part I: theory. *J. Sound Vib.* **227**, 555–586 (1999).

Acknowledgements

This work was financially supported by the Research Grants Council, the Hong Kong Special Administration Region Government, China, under the Project Nos. 152172/19E. Authors are grateful for this support. The funder played no role in study design, data collection, analysis and interpretation of data, or the writing of this manuscript. Authors would also like to thank anonymous reviewers for their insightful comments.

Author contributions

W.K.L. wrote the original manuscript, prepared all figures and tables, collected data, implemented the methodology, and conducted formal analysis and software simulations and validation. A.K. contributed to conceptualization, supervision, investigation, resources, methodology, and funding acquisition. O.U. assisted with the investigation. S.K.T. handled funding acquisition, project administration, resources, and supervision. All authors reviewed and edited the manuscript.

Competing interests

The authors declare no competing interests.

Additional information

Supplementary information The online version contains supplementary material available at https://doi.org/10.1038/s44384-025-00026-5.

Correspondence and requests for materials should be addressed to Wai Kit Lam.